scientific reports

Check for updates

OPEN

Self-organized angleworm-like and centipede-like patterns in ac-driven electroconvection of nematic liquid crystals

Jong-Hoon Huh

We report localized electroconvection (EC) discovered in nematic liquid crystals (NLC), which resembles life-like angleworms (AW) and centipedes (CP) in nature. In the presence or absence of superposed noise on an ac field, such localized EC patterns are self-organized. We investigated their spatial and dynamical features in terms of the spontaneous formation and evolution of patterns. In a planarly-aligned NLC cell, the AWs are discovered in the conduction ($f<f_{cd}$) and dielectric ($f>f_{cd}$) regimes which are divided by a characteristic frequency f_{cd}. Moreover, in a homeotropically-aligned NLC cell, two types of the CP (i.e., single CP and couple CP) are discovered slightly before f_{cd}. Considering the director field of NLC in the noise and/or ac fields, we explain the emergence of these noticeable dissipative structures that are not conventional wholly-occupying patterns in systems but localized ones, and that are not stationary but regularly dynamical. It is crucial to consider the redistribution of electric charges through additional noise effects or disclinations of NLC.

Liquid crystals are highly useful materials, and are now found in high-performance smart displays[1]. They are also an attractive system for studying the formation and evolution of patterns in nonequilibrium dissipative systems[2]. AC-driven electroconvection (EC) in nematic liquid crystals (NLC) has been extensively investigated to understand nonequilibrium physics over the last six decades [1–4] since Williams domains were observed in NLC[5]. The EC turned out to be an electrohydrodynamic instability by Carr and Helfrich[6,7]. The electric potential difference between a thin NLC layer drives EC in an anisotropic fluid (i.e., NLC) through the Coulomb force acting on the positive and negative charges that are inhomogeneously distributed by the anisotropy of electric and visco-elastic properties due to rodlike molecules. It is similar to the temperature difference that drives Rayleigh – Bénard convection in (usual) isotropic fluids through buoyancy to the lighter fluid and through gravity to the heavier one resulting from the density variation[8]. In fact, the EC provides a wide variety of dissipative structures from regular normal rolls (NR) to spatio-temporal chaos, from stationary waves to traveling waves (TW), and from wholly-occupying to localized patterns[4,9–11,12]. These various ECs are generated by secondary instabilities [9–11,12] with the primary Carr – Helfrich instability[6,7]. In particular, localized EC patterns were observed in low conductivity cells[9], in laser-induced systems[10], and in two superposed ac fields with different frequencies[11].

In principle, the director and velocity fields in EC are governed by the torque balance for the director and the momentum balance in the Navier – Stoke's equation, respectively. In general, the director $\boldsymbol{n}$ is defined by the locally averaged orientation of the rodlike molecules of NLC ($\boldsymbol{n} \equiv -\boldsymbol{n}$; $|\boldsymbol{n}|=1$)[1,3]. For EC, a rest state can be destabilized by applying an ac voltage $V(t) = E(t)d = \sqrt{2}V \cos 2\pi f t$ across an NLC layer (typically, thickness $d = 10$–100 μm) sandwiched between two parallel electrodes [$\boldsymbol{E}(t)$ // $\hat{\boldsymbol{z}}$], as shown in Fig. 1a. Accordingly, at a critical voltage V_c, well-ordered NR (i.e., a kind of Williams domains) with a wave number $\boldsymbol{k}_{NR}$ parallel to the initial director $\boldsymbol{n}_0$ (//$\hat{\boldsymbol{x}}$) is observed under a polarizing microscope[3,4]. For the low-frequency conduction regime ($f<f_{cd}$), one finds that $V_c \propto (1+4\pi^2 f^2 \tau_\sigma^2)/[\zeta^2 - (1+4\pi^2 f^2 \tau_\sigma^2)]$, in which τ_σ ($=\varepsilon_0\varepsilon_\perp/\sigma_\perp$) and ζ^2[$=(1-\sigma_\perp\varepsilon_{||}/\sigma_{||}\varepsilon_\perp)(1+\alpha_2\varepsilon_{||}/\eta_1\varepsilon_a)$] denote the charge relaxation time and the Helfrich parameter including viscous properties (α_2 and η_1) and dielectric anisotropy ($\varepsilon_a = \varepsilon_{||} - \varepsilon_\perp$) [1–67]. Here, f_{cd} indicates a characteristic frequency dividing the conduction ($f<f_{cd}$) and dielectric ($f>f_{cd}$) regimes[3,4], as shown in Fig. 1b.

The typical EC evolution from a primary EC (i.e., NR or oblique rolls depending on the ac frequency $f<f_{TW}$) to the so-called dynamic scattering mode (DSM) is well understood[4,13,14]; it includes irregular dynamics such as defect chaos[16,17]. Furthermore, for higher f (i.e., $f_{TW}<f<f_{cd}$), TW arises at V_c and also evolves into the DSM[4,13]

Department of Physics and Information Technology, Faculty of Computer Science and Systems Engineering, Kyushu Institute of Technology, Fukuoka 820-8502, Japan. email: huh@phys.kyutech.ac.jp

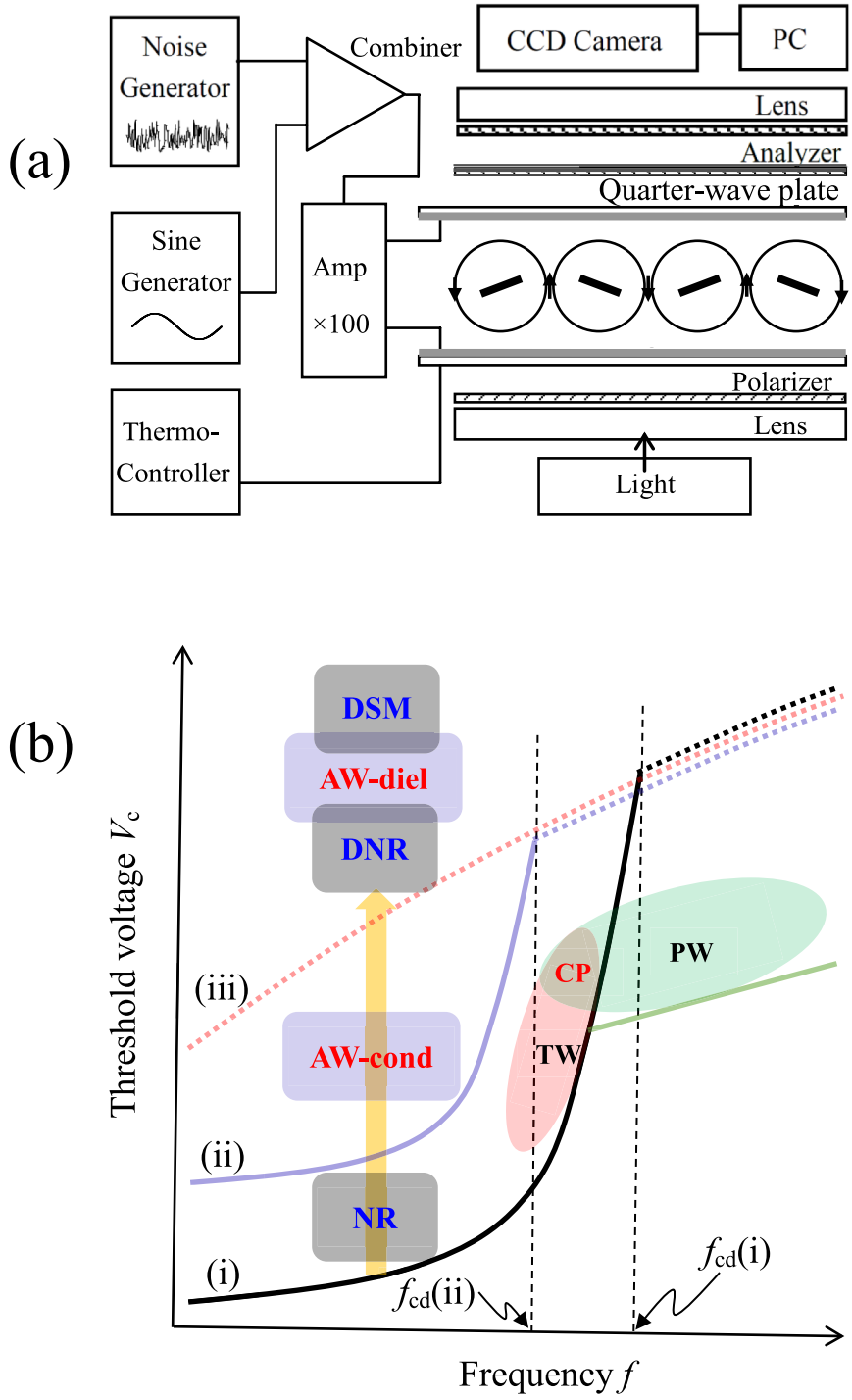

Fig. 1. (**a**) Experimental setup. The periodic rods between two parallel transparent electrodes indicate the director ***n*** of a nematic liquid crystal (NLC), and the circles indicate vortices of electroconvection (EC). (**b**) Sketch of threshold voltage V_c with respect to various noise intensity V_N. The well-established Carr–Helfrich threshold for EC [(i) for $V_N = 0$] smoothly shifts to higher voltages [(ii) for $0 < V_N < V_N^*$] by increasing V_N[1234], and then remains only in the dielectric regime for high intensity V_N [(iii) for $V_N > V_N^*$]; here, V_N^* indicates a characteristic intensity determining a transition between the conduction and dielectric regimes. The pattern evolution [NR (normal roll) → AW-cond → DNR (dielectric normal roll) → AW-diel → DSM (dynamic scattering mode)] is found by increasing V_N (along the thick arrow), as shown in Fig. 3; here, AW-cond and AW-diel indicate angleworm-like patterns (AWs) in the conduction and dielectric regimes, respectively [i.e., Fig. 3(g) and 3(j)]. Moreover, a prewavy pattern (PW) can be overlapped with traveling waves (TW), providing the background of the centipede-like pattern (CP) (Fig. 5(c)).

(Fig. 1b); regular dynamics can be determined as a phase velocity or Hopf frequency[18–20,13,21]. For much higher f ($>f_{cd}$), on the other hand, a different EC called pre-chevrons [or dielectric NR (DNR)], which is characterized by k_{DNR} much larger than k_{NR}, is observed at V_c, and then it develops into chevron patterns by increasing V; one can confirm that $V_c \propto f^{1/2}$ [3,4,22,23,24].

In this paper, we present two life-like EC patterns resembling angleworms (AW) and centipedes (CP), which move like real ones. Note that they are spontaneously formed in order of micro-scale by using nano-scale elements (i.e., molecules of the present NLC used in this study). Moreover, they are clearly localized in space; this should be distinguished from usual EC patterns that are wholly-occupying the active area S of the cell ($S = 1$ cm $\times$ 1 cm in this study). In particular, animating AW and CP are examined by considering the TW. The dynamics of AW and CP requires an AC field with a frequency within a specific range ($f_{TW} < f < f_{cd}$), where TWs induce moving rolls through a Hopf instability (Fig. 1b); if needed, additional noise superposed on the ac field is introduced. In addition, the AW is compared with the so-called "worms (or solitons)" reported previously as localized EC patterns in one-[21,25] and two- [9–11,13] dimensional systems. The evolution process through self-organization occurs by collaborative equilibrium and nonequilibrium effects. In fact, the CP arises on the brink of EC extremely close to an equilibrium state. Although the present AW and CP are far from animating real creatures, they indicate possible emergence of a world showing highly organized-dissipative structures in nature[26,27].

We aim to show the AW and CP by analyzing their director fields, and to reveal their formation mechanisms. Our study suggests that such a dissipative system (e.g., EC) plays a crucial role in the formation and evolution of patterns into complex structures out of simple aggregations of molecules. Such emergence of localized patterns should be distinguished from phase transitions between homogeneous states in conventional equilibrium systems [28] , and from the pattern evolution between nonequilibrium states that are wholly-occupying in systems [2–4]. Thus, our findings may help understand the formation and evolution of countless patterns in nature and be a useful means of self-organization in nanotechnology.

Materials and methods

A typical thermotropic NLC, *p*-methoxybenzylidene-*p*-*n*-butylaniline (MBBA), was used in this study[1,3]. The NLC was injected into two types of sample cells: a planarly-aligned director cell with $\boldsymbol{n}_0 = (1,0,0)$ at $z = 0$ and $z = d$ (Fig. 2a), and a homeotropically-aligned director cell with $\boldsymbol{n}_0 = (0,0,1)$ at $z = 0$ and $z = d$; see Fig. 4a below. The details of the two cells are described in Table 1. As shown in Fig. 1a, the shadowgraph method was used for optical observations and measurements for EC[3,4]; if needed, a polarizer (P), an analyzer (A), and a quarter-wave plate (Q) were used in a polarizing microscope, which were set to be parallel, perpendicular, and $\pi/4$ to

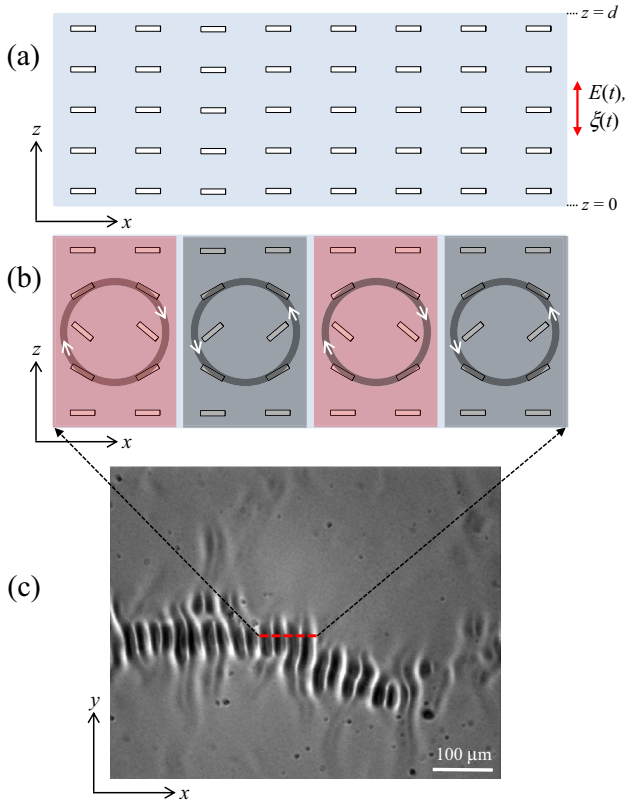

Fig. 2. Planarly-aligned cell for $V < V_c$ (**a**), the director field of EC for $V > V_c$ (**b**), and an AW pattern at an ac voltage $V = 62$ V ($f = 30$ Hz) above a threshold voltage V_c and additional noise intensity $V_N = 54$ V (**c**). The director field and vortices in (b) are well known in previous studies [1–4,32,50]. In principle, the AW in (c) is a localized dissipative structure evolved from NR (Fig. 3(a)); see the successive evolution into such AWs in Fig. 3.

Cell	Conductivity ($10^{-7}\Omega^{-1}$ m^{-1})		Dielectric constant		Cell thickness (μm) ± 5%
	$\sigma_{//}$	$\sigma_{\perp}$	$\varepsilon_{//}$	$\varepsilon_{\perp}$	d
P	0.90	0.61	4.1	4.5	50
H	6.3	5.4	4.5	5.3	25

Table 1. Two sample cells: the planarly-aligned cell (P) with $\boldsymbol{n}_0 = (1,0,0)$ and homeotropically-aligned cell (H) with $\boldsymbol{n}_0 = (0,0,1)$; see their corresponding director fields illustrated in Figs. 2a and 4a. The values were measured at $T = 25$ °C.

the x axis, respectively[23,24]. In the PQA condition referred to in this paper, the light propagates successively along the route: light source → lens → P → cell → Q → A → lens → CCD camera (Fig. 1(a)); if the A is replaced by another P, this is referred to as the PQP. In particular, the PQA and PQP conditions uncover clockwise- and counterclockwise-twisted directors along the z axis[23,24]. Moreover, if needed, the PA and PP conditions without the Q in the route were used, which are referred to as the (usual) crossed nicol and parallel nicol[29]. Furthermore, an additional noise voltage was used, which was superposed on the ac voltage $V(t)$; it was characterized by its intensity $V_N = \sqrt{< \xi^2(t) >}$ for which $\xi(t)$ was Gaussian white noise[12,33]. The patterns and their dynamics were observed using computer-controlled image software (Scion Image) together with a charge-coupled device (CCD) camera (Sony, XC-75) with a rate of 30 fps mounted on a polarizing microscope (Olympus, ML9300); the velocities of AWs and CPs was measured using the soft for dynamic image analysis. All observations and measurements were carried out at a fixed temperature ($T = 25$ °C). The details of the experiment were described in our previous papers[13,12,24].

Results

Angleworms (AW) in a planarly-aligned cell

(i) Evolution process to AW in the presence of noise

A typical NR ($\boldsymbol{k}_{NR}$ // $\boldsymbol{n}_0$ // $\hat{\boldsymbol{x}}$) was observed in the planarly-aligned cell (Fig. 2(a)). In the absence of noise ($V_N = 0$), the NR was well-organized in the entire cell (Fig. 3(a)). When using the additional noise of V_N, a locally-occupied structure resembling an AW was observed as shown in Fig. 2c. Obviously, it originates from EC (i.e., NR), providing a similar wave vector $\boldsymbol{k}_{AW}$ that smoothly increases with V_N[12]. In addition, Fig. 2b shows the director field and two vortex pairs of the NR, which is a typical figure of EC in the xz plane [1–4]. However, note that the director field and vortices are locally limited in the AW (Fig. 2(c)).

To see the process of pattern formation of the AW, the successive change of the patterns is displayed in Fig. 3; the early stage of the pattern evolution was already reported from a different viewpoint[12,34]. By increasing V_N [at fixed values of $\varepsilon = [V^2 - V_c^2(V_N)/V_c^2(V_N)] \approx 0.1$ and $f = 30$ Hz], a typical NR (Fig. 3(a)) gradually evolves into AW (Fig. 3(g)) via transient patterns (Fig. 3(c)–(f)) after a fluctuating Williams domain (or defect chaos) (Fig. 3(b)), and finally, the AW develops into turbulence (Fig. 3(l)). In this evolution process, noise plays a crucial role in the localization of EC[12,34]. The electric charges may begin to be redistributed from those of the conventional NR by the additional noise effects, and they may be reinforced by increasing V_N. In other words, the noise may cause a difference of the threshold voltages (V_c) between the inside and outside of the localized EC regions by the rearranged charge distribution. In the present case, V_c for the inside is lower than that for the outside; this indicates that the electric conductivity σ in the EC regions is higher than that in the EC-free region[13]. In other words, charges may be abnormally accumulated in the EC regions by the noise field. Therefore, owing to the sufficient localized-charge redistribution, the AW can be realized (Fig. 3(g)) via transient patterns due to insufficient localization of charges (Fig. 3(c)–(f)); obviously, the pattern evolution was determined in the conduction regime ($f < f_{cd}$) (Fig. 1(b))[3,4].

(ii) AWs in the conduction and dielectric regimes

On the other hand, upon increasing V_N [> 70 V] further, the noise field leads EC to the dielectric regime ($f > f_{cd}$)[34]; see a DNR (Fig. 3(i)) distinguishable from the NR (Fig. 3(a)) ($k_{DNR} \gg k_{NR}$) and note the coexistence of the AW and DNR in Fig. 3h. After a transition from the conduction regime ($f < f_{cd}$) to the dielectric regime ($f > f_{cd}$) by the noise, the AW disappears for a moment (Fig. 3(i)), and then immediately reappears (Fig. 3(j)); finally, the so-called DSM (Fig. 3(l)) is realized through increasing the number of AWs (Fig. 3(k)). The pattern evolution (Fig. 3(i)–(l)) was observed over the course of time (about 30 s) at a fixed $V_N = 70$ V (and $\varepsilon \approx 0.1$ and $f = 30$ Hz). In comparison with the AW in the conduction regime (Fig. 3(g)), the length of AW in the dielectric regime (Fig. 3(j) and (k)] is shorter on average while the widths are almost the same.

The noise-induced pattern evolution can be explained as shown in Fig. 1b; the Carr–Helfrich threshold curve V_c ($f < f_{cd}$, $V_N = 0$) smoothly shifts to higher voltages by increasing V_N, and then it appears to lose its conduction regime ($f < f_{cd}$) for sufficiently high V_N causing $f_{cd} \to 0$ [(iii) in Fig. 1(b)]; in other words, V_c remains only for the dielectric regime ($f > f_{cd}$) in the case of high V_N ($> V_N^* \approx 63$ V in this study). With increasing V_N (along the thick arrow) in Fig. 1(b), the pattern evolution [NR → AW-cond → DNR → AW-diel → DSM] (Fig. 3) is found by the noise-induced charge redistribution; here, AW-cond and AW-diel indicate AWs in the conduction and dielectric

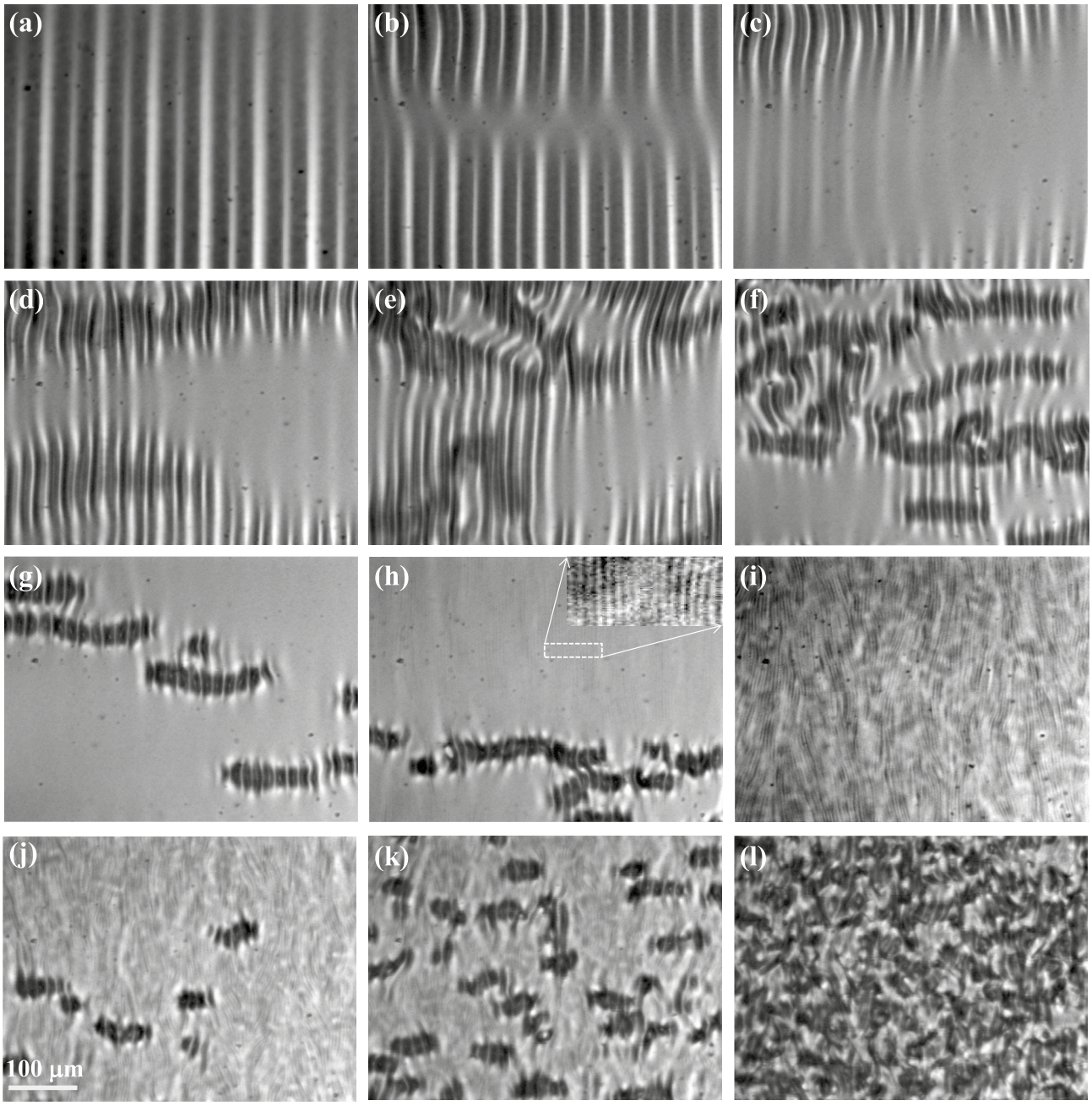

Fig. 3. Pattern evolution from NR (**a**) to AW (**g**), and to turbulence (DSM) (l) by increasing V_N (= 0–70 V) superposed on $V(t)$ [at fixed values of $\varepsilon = (V^2 - V_c^2(V_N)/V_c^2(V_N)) \approx 0.1$ and $f = 30$ Hz]; (**a**) $V_N = 0$ V, (**b**) 5.5 V, (**c**) 18 V, (**d**) 23 V, (**e**) 25 V, (**f**) 35 V, (**g**) 54 V, (**h**) 63 V, and (**i**) 70 V. At a fixed value of $V_N = 70$ V ($\varepsilon \approx 0.1$ and $f = 30$ Hz), the pattern [(**i**)] evolves into turbulence [(**l**)] via transient patterns [(**j**) and (**k**)] with time (during 30 s). Note that the wholly-occupying NR in the cell [(**a**) and (**b**)] is destabilized by increasing V_N [(**c**)–(**f**)] and sufficiently localized EC (i.e., AW) is clearly observed for appropriately large intensity V_N [(**g**) and (**h**)]. However, a different EC arises by increasing V_N [(**i**)]; that is, the noise gives rise to a dielectric EC called DNR that coexists in (**h**); see the magnified DNR in (**h**). After the DNR (i.e., pre-chevrons) without AWs [(**i**)], AWs reappear on the DNR [(**j**)] and the number of AWs increases [(**k**)]; finally, it develops into turbulence [(**l**)] with the generation of a huge number of AWs. The turbulence appears to be indistinguishable from the so-called dynamic scattering mode (DSM). See also Fig. 1(b).

regimes, respectively, and correspond to the AWs in Figs. 3(g) and 3(j). Both AWs appear to be conduction EC by charge redistribution, although EC-free and DNR regions are set as backgrounds for AW-cond and AW-diel, respectively. Details of the AWs such as their lengths and widths will be examined in a future study.

(iii) Traveling AW

On the other hand, the AWs actively move along the orientation of their length parallel to the initial director $\boldsymbol{n}_0$ (// $\hat{\boldsymbol{x}}$) if ignoring the slightly different orientation in Fig. 3g and k; for example, the velocity $\boldsymbol{v}$ of an AW was measured to be $|v_x| \sim 5.0$ μm/s = $0.1d$/s and $v_y \approx 0$ at $V_N = 70$ V (at $\varepsilon \approx 0.1$ and $f = 30$ Hz), although it depends on V, f, and V_N. Such motion may be explained by considering TW found at high frequencies near f_{cd} (i.e., $f_{TW} < f < f_{cd}$), as shown in Fig. 1(b)[18–2021]; a characteristic frequency f_{TW} is determined ($f_{TW} < f_{cd}$), and a Hopf frequency f_H ($\propto \sigma^{-1/2} d^{-3}$) characterizing the dynamics of TW becomes nonzero ($f_H \neq 0$) for $f > f_{TW}$ unlike stationary NR ($f_H = 0$) for $f < f_{TW}$. In other words, the dynamic feature of the AWs may result from a Hopf instability [18–203536]. In Fig. 1(b), by increasing V_N, the threshold curve $V_c(f)$ also shifts to the low-frequency side through decreasing f_{TW} and f_{cd}. For appropriately large V_N, if the main ac frequency f (= 30 Hz in this experiment) becomes larger than f_{TW} (i.e., $f > f_{TW}$), the AWs become a localized TW13; that is, the superposed noise can cause such a Hopf instability in EC through the charge redistribution resulting in the variation of the threshold curve $V_c(f)$. Moreover, regarding the motion of the AWs, they combined and divided randomly, but did not cross each other.

(iv) Comparison with similar AWs in other studies.

It is worth mentioning here similar AWs discovered by other researchers [9,1011]. Dennin et al. reported localized TW states (worms) that are nearly equivalent to our AW in terms of the structure and dynamics including moving orientations[9]; although the worms were determined in the absence of noise, they could be induced and explained by coupled complex Ginzburg–Landau equations considering four modes (i.e., right- and left-traveling and stationary zig and zag rolls)[18,1920]; note that conductivity σ plays a crucial role for them, as for our AW. Moreover, Giebink et al. examined laser-induced EC pulses in the absence of noise that were also nearly equivalent to our AW from the same viewpoint mentioned above[10]; note that the laser-originated local conductivity variation for the pulses resulting from the change in temperature in the laser beam is replaced by the noise-induced charge redistribution for our AW. On the other hand, Éber et al. observed localized EC structures in two superposed ac voltages with different frequencies (in the absence of noise) 11; obviously, the orientation of the structures differs from that of our AW, worms, and pulses stated above; that is, the length direction of the former is perpendicular to $\boldsymbol{n}_0$ (i.e., $\boldsymbol{k} \perp \boldsymbol{n}_0$) but that of the latter is parallel to it (i.e., $\boldsymbol{k}$ // $\boldsymbol{n}_0$); the two ac voltages with different frequencies may cause a complicated charge distribution that allows the structures to be formed. Obviously, these similar AWs as well as our AW show a common feature that EC regions with higher σ (and lower V_c) are separated from EC-free regions with lower σ (and higher V_c).

Centipedes (CP) in a homeotropically-aligned cell

(i) Evolution process to CP in the absence of noise

In the case of the homeotropically-aligned cell (Fig. 4(a)), EC arises through two steps, as shown in Fig. 4[3738]. The initial director $\boldsymbol{n}_0$ (// $\hat{\boldsymbol{z}}$) first experiences the so-called Fredericks transition for $V > V_F$ ($= \sqrt{K_{33}/\varepsilon_0 \varepsilon_a} \sim 4$ V for MBBA with the elastic constant of bending $K_{33} \sim 7.5 \times 10^{-7}$ dyn) (Fig. 4(b)), independent of f; then, EC arises for $V > V_c > V_F$, dependent on f[1,3]. In principle, the Carr–Helfrich threshold $V_c(f)$ is equivalent to that for the planarly-aligned cell[4]; however, the wave vector $\boldsymbol{k}$ of the typical EC (i.e., the so-called soft-mode turbulence 37) has locally random orientations, which critically differs from that of the NR for the planarly-aligned cell ($\boldsymbol{k}_{NR}$ // $\boldsymbol{n}_0$ //$\hat{\boldsymbol{x}}$)[3738]. In the first step (i.e., during the Fredericks transition), unexpected director fields appear, providing disclinations resulting from the arbitrary orientations of the tilting directors[1,3]. In other words, since the tilting orientations of the director in the xy plane cannot be uniquely determined at the Fredericks transition (Fig. 4(b)), many disclinations appear if one does not increase V with infinitely slow and small steps. In fact, such disclinations disappear after enough time for minimizing the Frank elastic energy [$f_e = -(1/2)\varepsilon_0 \varepsilon_a (\boldsymbol{E} \cdot \boldsymbol{n})^2$] for NLCs having negative ε_a (for MBBA)[1,3]. However, in the usual experimental time scale for EC (i.e., order of hours), each disclination may be topologically stable[1,3], as dislocations do in normal crystals[39].

Usually, the EC including disclinations is driven by a coupling effect between the convective mode (i.e., $\boldsymbol{k}$) and the in-plane rotation mode of the director (i.e., $\boldsymbol{C}$-director) that is defined by the projection of $\boldsymbol{n}$ in the xy plane[37,38]. Unusually, if one increases V slowly against active disclinations in the Fredericks state, EC can arise only around them, as shown in Fig. 4c and d; this is because the threshold V_c^* around disclinations is slightly lower than V_c outside them. Similar to the AW (Fig. 3(g)), the localized spaces around disclinations may have larger conductivity for V_c^* lower than V_c of the usual EC ($V_c^* \approx 105$ V and $V_c \approx 112$ V at $f = 1$ kHz); that is, unusual deformation of the director in disclinations may cause unusual charge focusing for EC; this point is similar to the noise-induced unusual charge distribution in the AWs. As a result, for $V_c^* < V < V_c$, a localized EC resembling CP in nature could be observed for the first time, as shown in Fig. 4d. Interestingly, the CP was determined as a couple, moving toward the same orientation and with the same velocity: e.g., $v_y = 5.99$ μm/s in the case of Fig. 4d [$V = 110$ V ($f = 1$ kHz) $> V_c^*$]; note that the x and y axes are arbitrarily determined in the homeotropically-aligned cell not having the preferred initial director in the xy plane.

To better understand the couple CP, the pattern evolution process is displayed in Fig. 5a–c, which was obtained in the crossed nicol condition by increasing V ($> V_F$). Figure 5a shows a kind of disclinations between two topological defects in the Fredericks state ($V_F < V < V_c^*$) where the director cannot be defined, like a kind of singularity[1,3]; usually, defects are characterized by strength or winding number s in $\Phi(\boldsymbol{r}) = s\alpha + \beta$. Here, $\Phi(\boldsymbol{r})$ denotes the orientation of the $\boldsymbol{C}(\boldsymbol{r})$-director in the xy plane, and $\alpha = \tan^{-1}(y/x)$ and β is a constant. In general, $s = \pm 1/2$ and ± 1 in NLCs, as illustrated in Fig. 6[140]. The strength s is determined by the number of times that the $\boldsymbol{C}$-director rotates around each defect when the defect is encircled; i.e., $\oint d\phi = 2\pi s (s = \pm 1/2, \pm 1, \pm 3/2, \pm 2 \cdots)$ [140]. Figure 5a shows disclinations with $s = \pm 1$, providing four brushes around the defects. The dark brushes are called Schlieren textures, which are satisfied with the transmitted optical intensity $I = I_0 \sin^2(2\phi)\pi n_a d/\lambda_{light}$

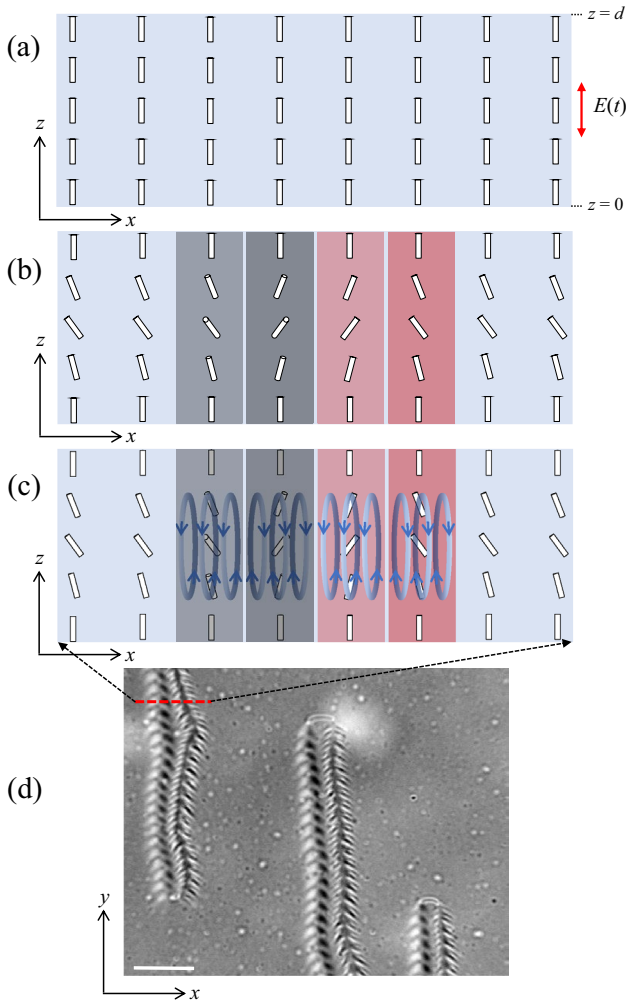

Fig. 4. Homeotropically-aligned cell for $V < V_F \sim 4.0$ V (**a**), Fredericks state with disclinations for $V_F < V < V_c^*$ (**b**), EC for $V > V_c^*$ (**c**), and CP at $V = 110$ V ($f = 1$ kHz) ($> V_c^* = 105$ V) (**d**). The director field and vortices in (c) are well known in previous studies[45032]. Two CPs in each couple have different director fields from each other [(**c**)] and different optical patterns [(**d**)]. Note that the left-handed CP has a set of clockwise- and counterclockwise-twisted directors along the z axis. In contrast, the right-handed CP has bending deformations in the director fields; see also Figs. 7 and 8a.

in the crossed nicol condition; here, n_a and λ_{light} indicate the anisotropy of refractive indices of the NLC and the wavelength of the incident light with intensity I_0, respectively[14041]. For $V > V_c^*$, the two defects become the head or tail for the couple CP, and the two line-disclinations serve as their backbones, as shown in Fig. 5b. Many couple CPs were observed by a small increase in V (Fig. 5(c)). In addition, note that each couple of the CPs consists of two different CPs exhibiting different optical patterns; compare the left-handed CP with the right-handed one in a couple in Figs. 4d and 5b; see below.

(ii) Two types of CP

Moreover, a different type of CP was observed in another pattern evolution process ($f = 700$ Hz), as shown in Fig. 5d–f. In the crossed nicol condition, two defects providing two brushes characterized by $s = \pm 1/2$ (Fig. 5(d)) are determined, which should be distinguished from those with $s = \pm 1$ (Fig. 5(a)). Consequently, the single CP occurs as shown in Fig. 5e; moreover, the velocity was measured to be $|\boldsymbol{v}| = 10.9$ μm/s at $V = 82$ V and $f = 700$ Hz. Similarly, many single CPs appear by a small increase in V (Fig. 5(f)). Note that the single CP is one of two CPs in a couple; optical patterns indicate that the right-handed CP in the couple (Figs. 4(d) and 5(b)) corresponds to the single CPs (Fig. 5(e)).

To obtain more information, the couple CP was observed in various optical conditions, as shown in Fig. 7. The two CPs that were indistinguishable in the parallel nicol condition (Fig. 7(c)) are clearly differentiated from each other in other conditions; see also Figs. 4d, 5b, and 5e. In fact, taking into account these optical images, the director field in the couple CP can be illustrated in the xz plane (Fig. 4(c)). In the left-handed CP in Fig. 7, the clockwise- and counterclockwise-twisted directors along the z axis are determined from their optical intensities, which are inverted in the PQA and PQP conditions (Fig. 7(a) and (b))[2324]. On the other hand, for the right-

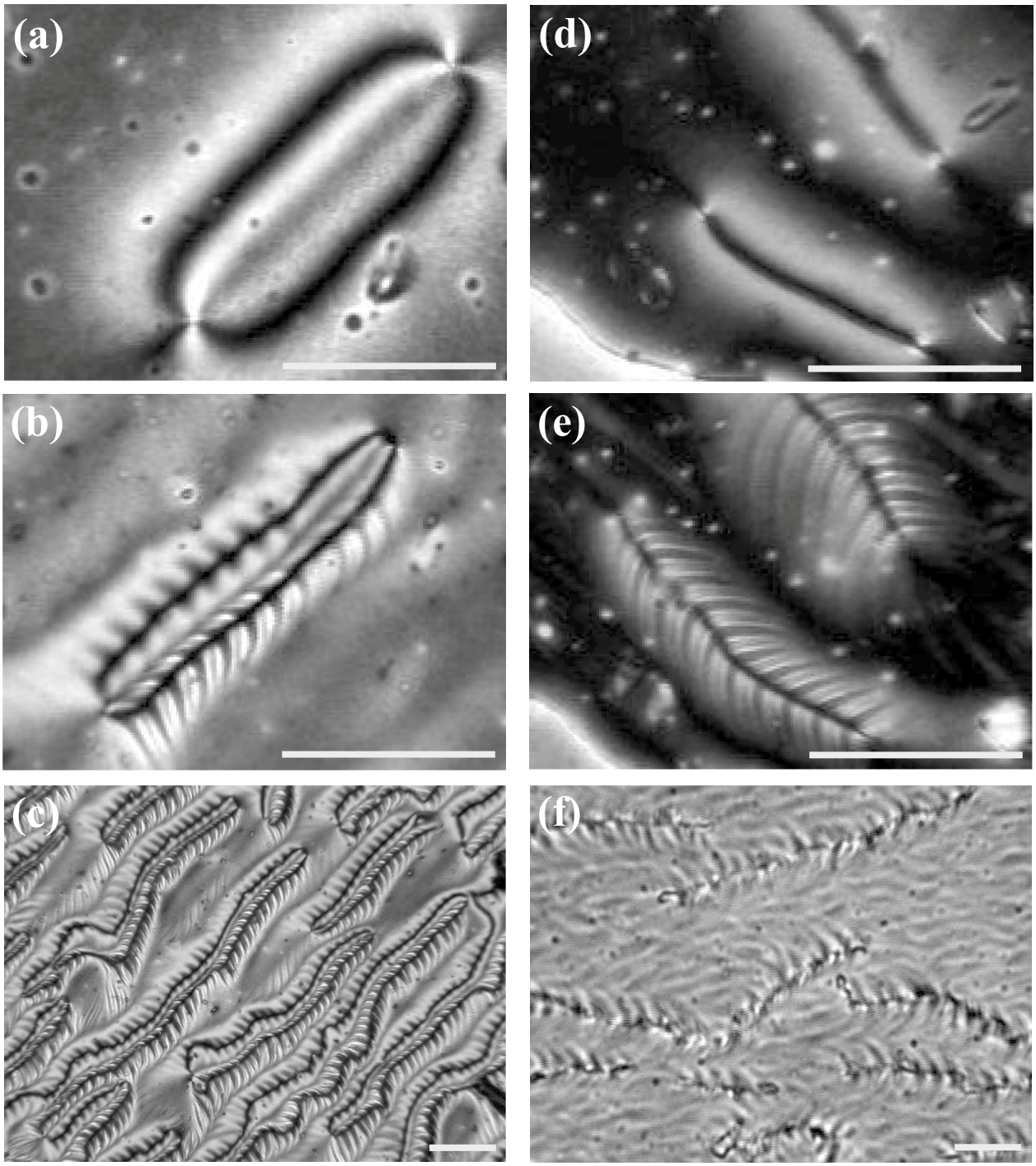

Fig. 5. Pattern evolutions from Fredericks state [(**a**)] to a couple CP [(**b**)] by increasing V (75–110 V at $f = 1$ kHz), and from the other Fredericks state [(**d**)] to single CPs [(**e**)] by increasing V (75–80 V at $f = 700$ Hz). Note that two types of CP exist; they are clearly distinguished by the so-called Schlieren textures with different numbers of brushes (i.e., four for the couple CP, and two for the single CP). By further increasing V [(**c**) at 120 V and (**f**) at 82 V], many couple and single CPs were generated. All pictures were obtained in the crossed nicol condition. See also Fig. 1(b) for understanding a background pattern (i.e., PW) of the couple CP [(**c**)]. The scale bars are 100 μm.

handed CP, the director is found to have bending modulation without the twisting mode (Fig. 4(c)) and their optical intensities are not inverted in the PQA and PQP conditions (Fig. 7(a) and (b)]; accordingly, one finds that both sides resembling legs of the CP have equivalent optical intensities in each condition (Fig. 7). In addition, it is found that the single CP is the same type as the right-handed one in the couple CP, showing the same director

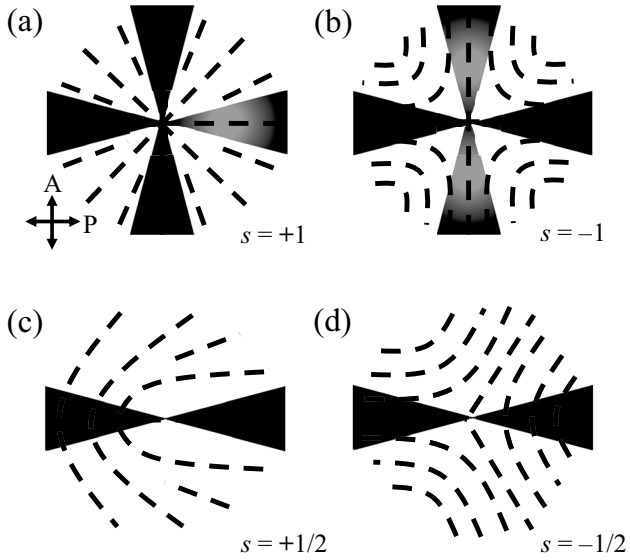

Fig. 6. Schematic images in the *xy* plane for the director fields around topological defects providing typical Schlieren textures ($s = \pm 1$ and $s = \pm 1/2$ if $\beta = 0$) characterized by the ***C***-director angle against the *x* axis [$\Phi(\boldsymbol{r}) = s\alpha + \beta$]. In principle, the Schlieren brushes are four at $s = \pm 1$ and two at $s = \pm 1/2$ in the crossed nicol condition; their dark optical intensity could be confirmed by $I \propto \sin^2(2\phi)$, as shown in Fig. 5(a) and (b).

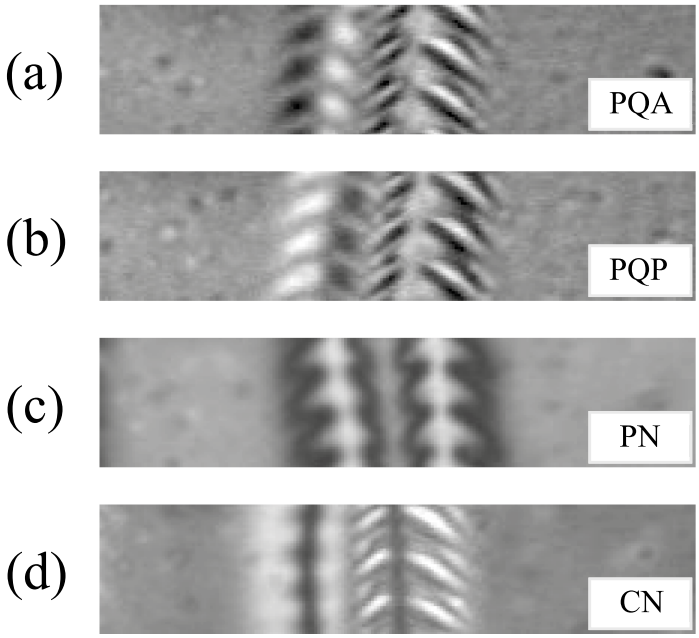

Fig. 7. Different optical images in four optical conditions: (**a**) PQA [crossed nicol with a quarter-wave plate (Q)], (**b**) PQP [parallel nicol with Q], (**c**) PN (parallel nicol without Q), and (**d**) CN (crossed nicol without Q); see also Fig. 1(a). Note that the left-handed CP shows different optical images in all conditions, and the images are inverted in PQA and PQP. This indicates that the left-handed CP has a set of clockwise- and counterclockwise-twisted directors along the *z* axis[23,24]. The PN [(**c**)] cannot distinguish the difference of two CPs in a couple.

modulation; see the two single CPs in Fig. 5e, which are the same as the right-handed CP in Figs. 5b and 7d in the crossed nicol condition.

To compare the two types of CP, the director fields of the disclination structures before EC (i.e., $V_F < V < V_c^*$) are illustrated as shown in Fig. 8. The couple CP is formed in a pair of twist-bend-directors as well as a pair of bend-directors (Fig. 8(a)); on the other hand, the single CP is formed only in a pair of bend-directors (Fig. 8(b)); both also contain the splay deformation around the defects. For the single CP, the comparatively

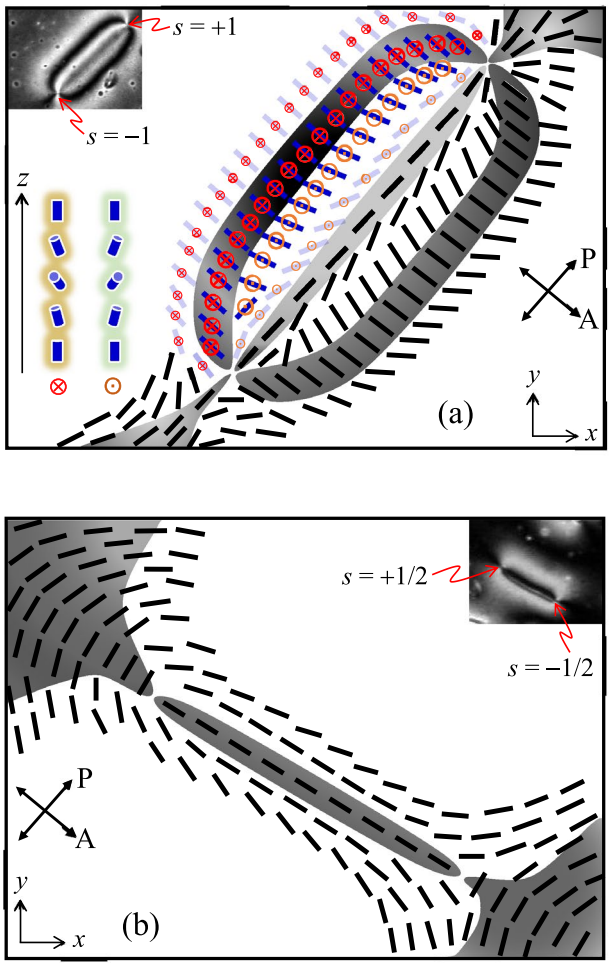

Fig. 8. The director fields (i.e., ***C***-director in the *xy* plane) in Schlieren textures to generate a couple CP (Fig. 5(b)) (**a**) and a single CP (Fig. 5(e)) (**b**). These can be determined from the well-known typical Schlieren textures and director fields (Fig. 6). The couple and single CPs are generated on the background of the Fredericks state providing disclinations with strength or winding number $s = \pm 1$ and $s = \pm 1/2$, respectively. Note that the left-handed disclination in (**a**) has a set of clockwise- and counterclockwise-twisted directors along the *z* axis; see the corresponding symbols ⊗ and ⊙ in (**a**); the size of the symbols denotes amplitude of the twist angle at $z = d/2$.

simple disclination with $s = \pm 1/2$ (Figs. 5(d) and 8(b)) is determined; in contrast, for the couple CP, complicated disclinations with $s = \pm 1$ (Figs. 5(a) and 8(a)) and an additional twist deformation for one of the two CPs (Figs. 7 and 8a) are found; in Fig. 8a, the symbols (⊗and ⊙) indicate clockwise- and counterclockwise-twisted directors along the *z* axis, respectively.

(iii) Traveling CP and different background states

In principle, two opposite defects with $s = \pm 1/2$ or ± 1 attract each other like electric charges, and annihilate by combining with each other in the Fredericks state[140]; however, they can maintain the distance (i.e., the length) in the CPs and lengthen it by increasing *V*. This feature of the CPs in the nonequilibrium state is considerably different from that in the equilibrium state (i.e., Fredericks state). Moreover, the CPs randomly combine and divide with their movements, but cannot cross each other. In addition, the velocity of the single and couple CPs was measured to be $|v| \sim (0.2 - 0.4)d/s$ in the case of $\varepsilon^* = (V^2 - V_c^{*2}/V_c^{*2}) \approx 0.1$; thus, the velocities of the AW and CPs are not so different from each other in the present study. As described for the AWs, the dynamic feature of the CP can also be explained as a Hopf instability for TW near f_{cd} (Fig. 1(b)). In other words, the CP is also a kind of localized TWs for $V_c^* < V < V_c$ and $f_{TW} < f < f_{cd}$. In the case of CP, the Hopf instability is induced only by high frequencies ($> f_{TW}$) without the aid of noise, whereas that in the AWs may be done by the noise (Figs. 1(b) and 3). As the velocity is determined by the Hopf frequency f_H ($\propto \sigma^{-1/2} d^{-3}$) [18–2021], it may be controlled by using different parameters σ and *d*. By superposing noise as was done for the AWs, the details of CP such as *v* as well as V_c, V_c^*, and f_{cd} are varied; this will be examined in a future study.

It is also interesting to consider the difference of the backgrounds of both CPs in Fig. 5c and f. In the case of the couple CP in Fig. 5c [and also Fig. 5(b)], the so-called prewavy pattern (PW, or wide domains)

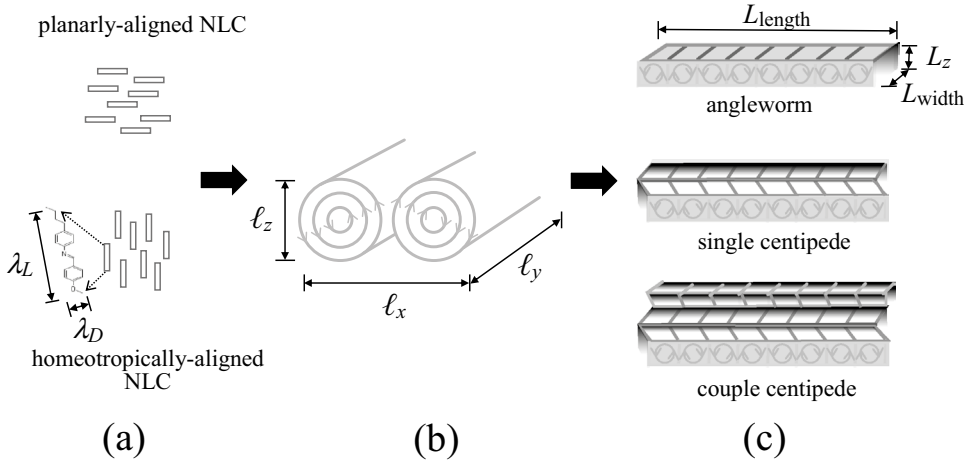

Fig. 9. Schematic view for successive evolutions to the localized EC (i.e., AW and CP). (**a**) The element of the present NLC (i.e., MBBA) in the planarly-aligned cell (Fig. 2(a)) and homeotropically-aligned cell (Fig. 4(a)), (**b**) a conventional EC [e.g., NR in Fig. 3(a)], and (**c**) the AW (Fig. 3(g)), single CP (Fig. 5(e)), and couple CP (Fig. 5(b)). See Table 2 for the characteristic sizes ($\lambda_{L,D}$, $\ell_{x,y,z}$, and $L_{\text{length, width}}$).

				AW		CP	
	Molecular (MBBA)	EC (TW)		Conduction regime	Dielectric regime	Single	Couple
Size	$\lambda_L \sim 25$ $\lambda_D \sim 4$ $\times 10^{-10}$ m	$\ell_x \sim 2d$ $\ell_y \sim S_y$ $\ell_z \sim d$	$L_{\text{length}} \sim$ $L_{\text{width}} \sim$ $L_z \sim$	$2d$–$30d$ $2d$ d	$2d$–$10d$ $2d$ d	$6d$–$50d$ $2d$ d	$6d$–$50d$ $4d$ d
Time scale	10^{-5} – 10^{-1}	$v \propto \sigma^{-1/2} d^{-2}$	$\lvert v \rvert$	0.1d /s	0.1d/s	0.4d/s	0.2d/s

Table 2. Characteristic sizes and times of the structures in successive steps for the pattern evolutions into the angleworm (AW) and centipede (CP) patterns determined in the ac-driven EC system (with cell thickness d and active area $S = S_x \times S_y = 1$ cm $\times$ 1 cm); see the definition of $\lambda_{L,D}$, $\ell_{x,y,z}$, and $L_{\text{length, width}}$ in Fig. 9.

is faintly shown as a background pattern[23,24,42,43,44]. In general, the PW is characterized by the clockwise- and counterclockwise-twisted directors along the z axis[23,24], and also it appears near f_{cd} as illustrated in Fig. 1b[4]. Thus, PW-superposed NR (called defect-free chevrons) appears in the case of no Hopf instability, whereas PW-superposed TW arises by the Hopf instability; see the overlapped region of TW and PW in Fig. 1b. Accordingly, the present couple CP can be interpreted as localized PW-superposed TW. Moreover, the moving orientation of the couple CP is determined by the PW as done by the initial director $\boldsymbol{n}_0$ for the AWs; see the moving CP along the bands of the PW in Fig. 5c. On the other hand, the present single CP (without such a twist mode) in Fig. 5d has no background such as the PW. Therefore, which of single and couple CPs appears is determined by the presence or absence of twist modes such as the PW. Although both CPs have been observed for the first time and their director structures and dynamics have been examined in this study, many questions remain such as the dimensions of their sizes (especially, their lengths); their combination and separation are left for future study.

Pattern evolution from simplicity to complexity

In addition, in terms of successive evolution from simplicity to complexity, the pattern evolutions for the AW and CP are described in Fig. 9 and Table 2. Our study suggests that in appropriately nonequilibrium states not too far from equilibrium states, a variety of complexity can be realized; such behavior may provide insight into general mechanism of self-organization in nonequilibrium physical systems. In equilibrium states, homogeneous NLC states (Figs. 2(a), 4(a), and 9(a)) are realized; moreover, in nonequilibrium states very far from equilibrium, homogeneous turbulent states [e.g., Fig. 3(l)] are found[2,4,14]. However, in appropriately nonequilibrium states not too far from equilibrium, wholly-occupying periodic patterns [e.g., Fig. 3(a)] are formed by the well-known electrohydrodynamic instability [2–4]; more interestingly, localized and animating patterns [e.g., Figs. 2(c) and 4(d)] resembling living creatures in nature can be generated by specific conditions (e.g., additional noise-induced or disclination-induced charge redistribution in this study). The macroscopic structures (Fig. 9(b) and (c)) in appropriately nonequilibrium states should be distinguished from the microscopic elements (Fig. 9(a)); moreover, the characteristic times differentiate the former from the latter, as seen in Table 2.

Finally, in the emergence of basic elements such as NLCs (Fig. 9(a)) for pattern evolution, although it is important to understand quantum physics and chemistry, the subsequent evolutions from the elements require different tools such as nonlinear and nonequilibrium physics dealing with the dissipative, macroscopic structures including patterns and rhythms[28], which are essential for diversity observed in nature. In particular,

the localization of patterns and rhythms is very important for the evolution to complexity; note the difference between conventional EC (e.g., NR) and present ECs (i.e., AW and CP).

Discussion and conclusion

Two localized animating life-like patterns in the EC system of NLCs have been discovered, which are called the AW and CP in this study. They were observed in the planarly- and homeotropically-aligned director cells, respectively. They should be distinguished from the conventional EC patterns that are wholly-occupying the entire cells (e.g., NR, TW, PW, and DSM)[4]. The AW can be generated by additional noise causing inhomogeneous charge redistribution against normal charge distribution for EC. On the other hand, two types of CP were determined; the single and couple CPs were clearly distinguished from each other. Our results show that they can respectively evolve from disclinations having a pair of defects with two ($s = \pm 1/2$) and four ($s = \pm 1$) brushes in Schlieren textures[14041]. The dynamic features of the AW and CP can be explained by considering TW that arises near f_{cd} dividing the conduction and dielectric regimes[3,4]. In particular, the AW and CP could be found in the overlapped regions of various instabilities such as TW, PW, and DNR; moreover, they show a common feature that EC regions with higher conductivity σ (and lower threshold V_c) are separated from EC-free regions with lower σ (and higher V_c); such a feature is consistent with similar AWs reported by other researchers [9,1011]. To conclude, the noise- and disclination-induced charge redistribution causes the localization of EC and the shift to TW ($f > f_{TW}$ through a Hopf instability); moreover, two types of AW (i.e., AW-cond and AW-diel) are determined for the conduction ($f < f_{cd}$) and dielectric ($f > f_{cd}$) regimes by the additional noise intensity V_N, and two types of CP are classified by the winding number s (i.e., single CP with $s = \pm 1/2$ and couple CP with $s = \pm 1$).

Novel successive pattern evolutions generating the AW and CP were observed by controlling the noise intensity or ac voltages; furthermore, their dimensions in each step of the evolution processes were discussed in terms of pattern evolutions from simplicity to complexity. However, the sizes of their lengths and widths were not fully explained; this topic will be examined in a future study. Moreover, future work will explore localized EC patterns under colored noise and non-Gaussian noise, which are expected to influence charge redistribution and pattern stability[3033]. We hope that this study will inspire researchers to exploit the evolution of complexity[4546] and to apply the concept of self-organization to nanotechnology[4748]. In particular, we hope that the localization of patterns and rhythms will become an active topic in the study of nonequilibrium dissipative systems, contributing to a deeper understanding of diversity and complexity in nature[4931].

Data availability

The data that support the findings of this study are available from the corresponding author upon reasonable request.

Received: 3 September 2025; Accepted: 29 October 2025
Published online: 27 November 2025

References

1. de Gennes, P. G. & Prost, J. *The physics of liquid crystals* (Clarendon Press, 1993).
2. Kai, S. *Pattern formation in complex dissipative systems* (World Scientific, 1991).
3. Blinov, L. M. & Chigrinov, V. G. *Electrooptical effects in liquid crystal materials* (Springer, 1994).
4. Eber, N., Salamon, P. & Buka, A. Electrically induced patterns in nematics and how to avoid them. *Liq. Cryst. Rev.* **4**, 101 (2016).
5. Williams, R. Domains in liquid crystals. *J. Chem. Phys.* **39**, 384 (1963).
6. Carr, E. F. Influence of electric fields on the molecular alignment in the liquid crystal p-(anisalamino)-phenyl acetate. *Mol. Cryst. Liq. Cryst.* **7**, 253 (1969).
7. Helfrich, W. Conduction-induced alignment of nematic liquid crystals: Basic model and stability considerations. *J. Chem. Phys.* **51**, 4092 (1969).
8. Cross, M. C. & Hohenberg, P. C. Pattern formation outside of equilibrium. *Rev. Mod. Phys.* **65**, 851 (1993).
9. Dennin, M., Ahlers, G. & Cannell, D. S. Chaotic localized states near the onset of electroconvection. *Phys. Rev. Lett.* **77**, 2475 (1996).
10. Giebink, N. C. et al. Dynamics of laser-induced electroconvection pulses. *Phys. Rev. E* **69**, 066303 (2004).
11. Éber, N. et al. Suppression of spatially periodic patterns by dc voltage. *Phys. Rev. E* **93**, 042701 (2016).
12. Huh, J.-H., Kuribayashi, A. & Kai, S. Noise-controlled pattern formation and threshold shift for electroconvection in the conduction and dielectric regimes. *Phys. Rev. E* **80**, 066304 (2009).
13. Huh, J.-H. Traveling waves and worms in ac-driven electroconvection under external multiplicative noise. *Phys. Rev. E* **95**, 042704 (2017).
14. Huh, J.-H. & Osoguchi, H. Formation of grid patterns in an ac-driven electroconvection system. *Phys. Rev. E* **101**, 062701 (2020).
15. Kai, S. & Zimmermann, W. Pattern dynamics in the electrohydrodynamics of nematic liquid crystals. *Prog. Theor. Phys. Supp.* **99**, 458 (1989).
16. Rossberg, A. G. & Kramer, L. Pattern formation from defect chaos - a theory of chevrons. *Physica D* **115**, 19 (1998).
17. Oikawa, N., Hidaka, Y. & Kai, S. Formation of a defect lattice in electroconvection of nematics. *Phys. Rev. E* **70**, 066204 (2004).
18. Treiber, M. & Kramer, L. Bipolar electrodiffusion model for electroconvection in nematics. *Mol. Cryst. Liq. Cryst.* **261**, 311 (1995).
19. Dennin, M., Treiber, M., Kramer, L., Ahlers, G. & Cannell, D. S. Origin of traveling rolls in electroconvection of nematic liquid crystals. *Phys. Rev. Lett.* **76**, 319 (1996).
20. Treiber, M., Eber, N., Buka, A. & Kramer, L. Travelling waves in electroconvection of the nematic phase 5: a test of the weak electrolyte model. *J. Phys. II France* **7**, 649 (1997).
21. Huh, J.-H. Origin of traveling rolls in electroconvection of nematic liquid crystals. *Phys. Rev. E* **97**, 042707 (2018).
22. Scheuring, M., Kramer, L. & Peinke, J. Formation of chevrons in the dielectric regime of electroconvection in nematic liquid crystals. *Phys. Rev. E* **58**, 2018 (1998).
23. Amm, H., Stannarius, R. & Rossberg, A. G. Optical characterization of chevron texture formation in nematic electroconvection. *Physica D* **126**, 171 (1999).
24. Shiomi, M., Choi, E.-J. & Huh, J.-H. Prewavy instability-originated dielectric chevrons of electroconvection in nematic liquid crystals. *Rev. E* **102**, 042704 (2020).

25. Horikawa, A. & Huh, J.-H. Traveling waves in one-dimensional electroconvection of nematic liquid crystals. *J. Phys. Soc. Jpn.* **88**, 034602 (2019).
26. Wolf, Y. I., Katsnelson, M. I. & Koonin, E. V. Physical foundations of biological complexity. *PNAS* **115**, E8678 (2018).
27. Goldenfeld, N. & Woese, C. Life is physics: Evolution as a collective phenomenon far from equilibrium. *Annu. Rev. of Condens. Matter Phys.* **2**, 375 (2011).
28. Jaeger, G. The ehrenfest classification of phase transitions: Introduction and evolution. *Arch. Hist. Exact. Sci.* **53**, 51 (1998).
29. Morimoto, K., Tsujioka, H., Kitagawa, D. & Kobatake, S. Photoreversible Interference Color Modulation to Multicolor in Photochromic Molecular Crystals. *Bull. Chem. Soc. Jpn.* **92**, 1299 (2019).
30. Huh, J.-H. Noise-induced threshold shift and pattern formation in electroconvection by controlling characteristic time scales. *Phys. Rev. E* **84**, 025302 (2011).
31. Michaelian, K. Thermodynamic dissipation theory for the origin of life. *Earth Syst. Dynam.* **2**, 37 (2011).
32. W. Pesch and U. Behn, Electrohydrodynamic Convection in Nematics, in *Patterns, Defects and Material Instabilities*, edited by D. Walgraef and N. M. Ghoniem (Springer, Berlin, 2001), pp. 33–89.
33. Huh, J.-H., Shiomi, M. & Miyagawa, N. Control of stochastic and inverse stochastic resonances in a liquid-crystal electroconvection system using amplitude and phase noises. *Sci. Rep.* **13**, 16883 (2023).
34. Huh, J.-H. Multiplicative noise-induced electrohydrodynamic pattern formations by controlling electric conductivity. *J. Phys. Soc. Jpn.* **85**, 024002 (2016).
35. Marsden, J. E. & McCracken, M. *The hopf bifurcation and its applications* (Springer-Verlag, 1976).
36. Tóth-Katona, T., Cauquil-Vergnes, A., Éber, N. & Buka, Á. Nonstandard electroconvection with Hopf bifurcation in a nematic liquid crystal with negative electric anisotropies. *Phys. Rev. E* **75**, 066210 (2007).
37. Kai, S., Hayashi, K. & Hidaka, Y. Pattern forming instability in homeotropically aligned liquid crystals. *J. Phys. Chem.* **100**, 19007 (1996).
38. Rossberg, A. G., Hertrich, A., Kramer, L. & Pesch, W. Weakly nonlinear theory of pattern-forming systems with spontaneously broken isotropy. *Phys. Rev. Lett.* **76**, 4729 (1996).
39. Olson, I. A., Shtukenberg, A. G., Kahr, B. & Ward, M. D. Dislocations in molecular crystals. *Rep. Prog. Phys.* **81**, 096501 (2018).
40. Urbanski, M. et al. Liquid crystals in micron-scale droplets, shells and fibers. *J. Phys. Condens. Matter* **29**, 133003 (2017).
41. Kleman, M. Defects in liquid crystals. *Rep. Prog. Phys.* **52**, 555 (1989).
42. Barnik, M. I., Blinov, L. M., Grebenkin, M. F. & Trufanov, A. N. Dielectric regime of electrohydrodynamic instability in nematic liquid crystals. *Mol. Cryst. Liq. Cryst.* **37**, 47 (1976).
43. Nasta, L., Lupu, A. & Giurgea, M. Characteristics of domains appearing in nematic liquid crystals below the threshold voltage of chevrons. *Mol. Cryst. Liq. Cryst.* **71**, 65 (1981).
44. Huh, J.-H., Hidaka, Y., Rossberg, A. G. & Kai, S. Pattern formation of chevrons in the conduction regime in homeotropically aligned liquid crystals. *Phys. Rev. E* **61**, 2769 (2000).
45. Nakouzi, E. & Steinbock, O. Self-organization in precipitation reactions far from the equilibrium. *Sci. Adv.* **2**, e1601144 (2016).
46. Pokroy, B., Kang, S. H., Mahadevan, L. & Aizenberg, J. Self-organization of a mesoscale bristle into ordered, hierarchical helical assemblies. *Science* **323**, 237 (2009).
47. Hua, Wu. & Briscoe, W. H. Morphogenesis of polycrystalline dendritic patterns from evaporation of a reactive nanofluid sessile drop. *Phys. Rev. Mater.* **2**, 045601 (2018).
48. Ariga, K. et al. Self-assembly as a key player for materials nanoarchitectonics. *Sci. Tech. Adv. Mater.* **20**, 51 (2019).
49. Prigogine, I. *An introduction to the thermodynamics of irreversible processes* (Wiley, 1967).
50. Lee, K.-W. & Poschel, T. Field-driven pattern formation in nematic liquid crystals: mesoscopic simulations of electroconvection. *RSC Adv.* **7**, 42218 (2017).

Acknowledgements

This study was partly supported by SMC Corporation. The author is also grateful to the Western Japan Nonlinear Science Association for valuable discussions that contributed to this work.

Author contributions

J. -H. Huh conceived the research and conducted the experimental examination as his original work.

Funding

This study was supported by JSPS KAKENHI Grant Numbers 22K03470 and 25K07169.

Declarations

Competing interests

The authors declare no competing interests.

Additional information

Correspondence and requests for materials should be addressed to J.-H.H.